Technical Report, Zenodo, doi: 10.5281/zenodo.3971232 (2020)

ISMIP6 future projections for the Antarctic ice sheet with the model SICOPOLIS

Ralf GREVE[1,2], Reinhard CALOV[3], Takashi OBASE,[4]
Fuyuki SAITO[5], Shun TSUTAKI[6], Ayako ABE-OUCHI[4]

[1]Institute of Low Temperature Science, Hokkaido University, Sapporo, Japan

[2]Arctic Research Center, Hokkaido University, Sapporo, Japan

[3]Potsdam Institute for Climate Impact Research, Potsdam, Germany

[4]Atmosphere and Ocean Research Institute, University of Tokyo, Kashiwa, Japan

[5]Japan Agency for Marine-Earth Science and Technology, Yokohama, Japan

[6]National Institute of Polar Research, Tokyo, Japan

Contact: R. Greve (greve@lowtem.hokudai.ac.jp)

August 23, 2020

Abstract

The Ice Sheet Model Intercomparison Project for CMIP6 (ISMIP6) brings together a consortium of international ice-sheet and climate modellers to simulate the contribution from the Greenland and Antarctic ice sheets to future sea-level rise. In this document (supplementary to Seroussi et al. 2020), we describe the ISMIP6 Antarctica Tier-1 and Tier-2 experiments carried out with the ice-sheet model SICOPOLIS. First, we conduct a paleoclimatic spin-up over the last glacial-interglacial cycle until the year 1990. In this spin-up, we employ a nudging technique for the topography and aim at optimizing the match between simulated and observed surface velocities by adjusting the amount of basal sliding for individual drainage systems. Then, we carry out a historical run to bridge the gap between 1990 and 2015. The future climate projections run from the beginning of 2015 until the end of 2100. Results reveal a non-uniform response of the Antarctic ice sheet: for both employed future climate scenarios (RCP8.5/SSP5-8.5, RCP2.6/SSP1-2.6), mass losses and gains occur, depending on the specific forcing (provided by CMIP5 and CMIP6 global climate models). This is due to the counteracting effects of increasing ocean temperature (leading to a loss) and increasing precipitation (leading to a gain). For RCP8.5/SSP5-8.5, the ensemble mean is a mass loss of 18.5 mm SLE (sea-level equivalent) by 2100, and for RCP2.6/SSP1-2.6 it is 8.4 mm SLE. However, the uncertainty range is quite large, including the possibility of a mass loss of more than 100 mm SLE under RCP8.5/SSP5-8.5.

1 Introduction

The Coupled Model Intercomparison Project Phase 6 (CMIP6) is a major international climate modelling initiative (Eyring et al. 2016). As a part of this project, the Ice Sheet Model Intercomparison Project for CMIP6 (ISMIP6) was devised to assess the likely sea-level-rise contribution from the Greenland and Antarctic ice sheets until the end of this century (Nowicki et al. 2016, 2020).

Seroussi et al. (2020) describe the set-up and results of the ISMIP6 projections for the Antarctic ice sheet. The ensemble of simulations is based on 21 sets of ice-flow simulations submitted by 13 international institutions. The design of the experiments is sketched in Fig. 1. An initial state of the ice sheet is produced by either assimilation or spin-up techniques or a combination of both (Goelzer et al. 2018, Seroussi et al. 2019). The initialization date varies between the different models (here 1990 CE). A single historical run with a forcing that can be chosen freely bridges the gap between the initialization and the start date of the projections in January 2015. All projections run from this date until December 2100. The atmospheric forcing consists of anomalies for the surface mass balance (SMB) and surface temperature (ST), derived from selected CMIP5 and CMIP6 global climate models (Barthel et al. 2020). The oceanic forcing is a parameterization for ice-shelf basal melting that depends on the thermal forcing at the ice–ocean interface, which, in turn, is derived by extrapolating the oceanic fields simulated by the climate models into the ice-shelf cavities (Jourdain et al. 2020). A parameterization for ice-shelf fracture triggered by surface melting (Trusel et al. 2015) is also tested.

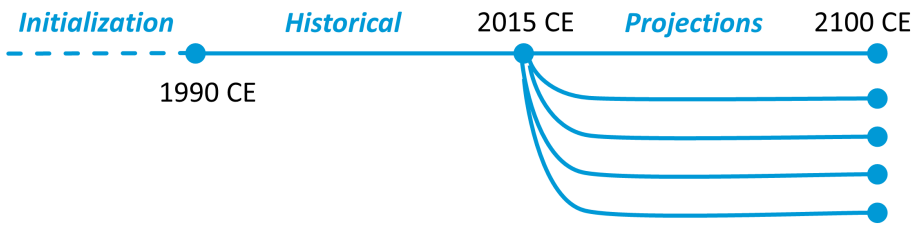

Figure 1: ISMIP6 experimental design. A model-specific initialization is followed by a historical simulation from 1990 until 2015. The several projections run from 2015 until the end of 2100. (Credit: Martin Rückamp, AWI Bremerhaven, Germany.)

Here, we describe the ISMIP6 future projections for the Antarctic ice sheet carried out with the ice-sheet model SICOPOLIS (SImulation COde for POLythermal Ice Sheets). The emphasis is on the model-specific features that are not covered in detail in the community papers (Seroussi et al. 2020, Payne et al. 2020). For the ISMIP6 future projections for the Greenland ice sheet, see the companion document by Greve et al. (2020).

2 Ice-sheet model SICOPOLIS v5.1

The three-dimensional, dynamic/thermodynamic model SICOPOLIS was originally created in a version for the Greenland ice sheet (Greve 1995, 1997a,b). Since then, the model has been developed continuously and applied to problems of past, present and future glaciation of Greenland, Antarctica, the entire northern hemisphere, the polar ice caps of

the planet Mars and others, resulting in more than 120 publications in the peer-reviewed literature (www.sicopolis.net, last accessed 2020-08-12).

Here, we apply SICOPOLIS v5.1 (Greve and SICOPOLIS Developer Team 2019) to the Antarctic ice sheet. The model domain covers the entire area of Antarctica and the surrounding oceans. We use the EPSG:3031 grid, based on a polar stereographic projection with the WGS 84 reference ellipsoid, standard parallel 71°S and central meridian 0°E. The stereographic plane is spanned by the Cartesian coordinates x and y, and the coordinate z points upward. It is discretized by a regular (structured) grid with $\Delta x = 8$, 16 or 32 km resolution. In the vertical, we use terrain-following coordinates (sigma transformation) with 81 layers in the ice domain and 41 layers in the thermal lithosphere layer below.

For the ice rheology, we use the regularized Glen flow law in the formulation by Greve and Blatter (2009, Sect. 4.3.2). Ice dynamics is modelled by the shallow-ice approximation (SIA) for slow-flowing grounded ice, hybrid shallow-ice–shelfy-stream dynamics for fast-flowing grounded ice and the shallow-shelf approximation (SSA) for floating ice. The hybrid dynamics is a modified form of Bernales et al.'s (2017) HS-1 scheme, for which the horizontal-velocity field v is computed as follows:

1. Compute the SIA solution with basal sliding (see below) $\rightarrow$ velocity v_{SIA}.

2. Slip ratio
$$r = \frac{v_{\mathrm{b,SIA}}}{v_{\mathrm{s,SIA}}} \tag{1}$$
(where subscripts 'b' and 's' refer to the base and surface, respectively).

3. Fast-flowing ice (streaming point) if $r > r_{\mathrm{thr}}$ (threshold slip ratio chosen as $r_{\mathrm{thr}} = 0.5$), then continue. Otherwise, use the SIA solution, $v = v_{\mathrm{SIA}}$.

4. Compute the solution for the shelfy-stream approximation (SStA) with the same basal-sliding law used for the SIA solution $\rightarrow$ velocity v_{SStA}.

5. Auxiliary factor
$$\tilde{r} = \frac{r - r_{\mathrm{thr}}}{1 - r_{\mathrm{thr}}} \quad (\in [0,1] \text{ for streaming points}) \,. \tag{2}$$

6. Weight factor
$$\check{r} = f_5(\tilde{r}) \,, \tag{3}$$
where the quintic function f_5 is defined by
$$f_5(x) = x^3 \left[10 - x(15 - 6\,x)\right] \tag{4}$$
(Fig. 2). Thus, for streaming points, $\check{r} \in [0,1]$.

7. Weighting
$$v = (1 - \check{r})\, v_{\mathrm{SIA}} + \check{r}\, v_{\mathrm{SStA}} \,. \tag{5}$$
Due to the staggered grid used by SICOPOLIS (Arakawa C grid, Arakawa and Lamb 1977), this must be done separately for the x- and y-components.

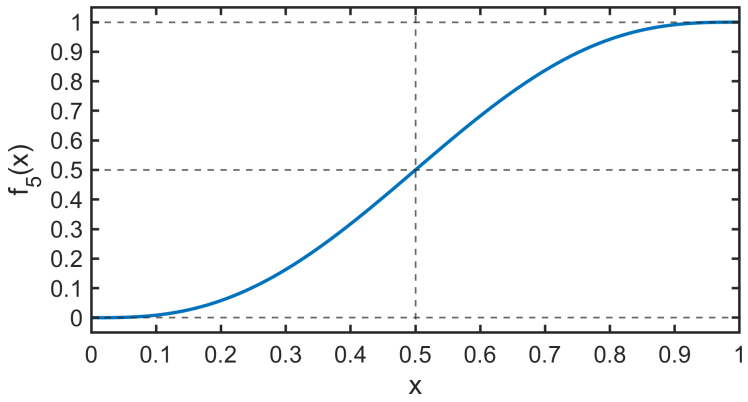

Figure 2: Quintic function $f_5(x)$ according to Eq. (4).

Compared to the original HS-1 scheme by Bernales et al. (2017), the new feature is using the quintic function f_5 in step 6 (SICOPOLIS parameter SSTA_SIA_WEIGH_FCT = 3). Since both the first and second derivatives of this function at the end points $x = 0$ and $x = 1$ are equal to zero, this guarantees a very smooth transition between slow- and fast-flowing grounded ice ($\check{r} = 0$) and between fast-flowing grounded and floating ice ($\check{r} = 1$).

In contrast to the SIA, the SStA and SSA require stress or velocity boundary conditions at the lateral margins of the domain. For the SSA, the boundary condition at the calving front states that the stress is equal to the hydrostatic pressure from the ocean water (e.g., Greve and Blatter 2009, Eqs. (6.62)–(6.64)). For the SStA, we distinguish between a marine-terminating and a land-terminating grounded ice front. For a marine-terminating front (in contact with the ocean), the boundary condition is essentially the same as for SSA/calving front; however, the floating condition is not fulfilled (a larger percentage of the ice column is above the water line). For a land-terminating front, we do not prescribe a stress boundary condition, so that the system merely sees the adjacent ice-free grid points with zero velocity (SICOPOLIS parameter BC_SSA_LTGF = 1). [The alternative, also implemented via BC_SSA_LTGF = 2, would be to impose a stress-free condition acting on the vertical face of the land-terminating front. However, this sometimes leads to unrealistically high velocities, so that we refrain from it.]

At the grounding line (transition between grounded and floating ice), we compute the surface (h) gradients at staggered-grid points by one-sided differences into either grounded or floating ice, depending on whether the staggered-grid points are grounded or floating (SICOPOLIS parameter GL_SURF_GRAD = 2). For instance, for the x-direction with grid index i, if the point i is grounded and the point $i+1$ is floating, then the gradient at the mid-point $i+\frac{1}{2}$ is discretized as

$$\left.\frac{\partial h}{\partial x}\right|_{i+1/2} \sim \begin{cases} \dfrac{h_{i+1/2} - h_{i-1/2}}{\Delta x}, & \text{if point } i+\frac{1}{2} \text{ grounded,} \\ \dfrac{h_{i+3/2} - h_{i+1/2}}{\Delta x}, & \text{if point } i+\frac{1}{2} \text{ floating.} \end{cases} \tag{6}$$

This is illustrated in Fig. 3. The decision whether the point $i+\frac{1}{2}$ is grounded or floating is done by linear interpolation of the ice topography between i and $i+1$. For the y-direction (grid index j), the scheme is analogous.

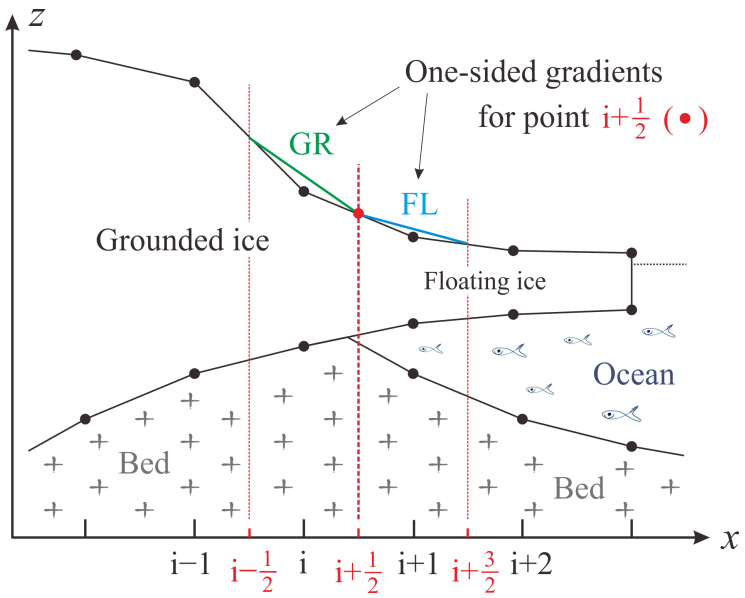

Figure 3: One-sided gradients of the discretized ice surface at the grounding line. Depending on whether the staggered-grid point $i + \frac{1}{2}$ is diagnosed as grounded or floating, either the one-sided gradient "GR" (pointing into the grounded ice) or "FL" (pointing into the floating ice) is used for $(\partial h/\partial x)|_{i+1/2}$.

Ice thermodynamics is modelled by the one-layer melting-CTS enthalpy scheme (Blatter and Greve 2015, Greve and Blatter 2016). The temperature-dependent rate factor for cold ice is by Cuffey and Paterson (2010, Sect. 3.4.6), and the water-content-dependent rate factor for temperate ice is by Lliboutry and Duval (1985).

The ice surface is assumed to be traction-free. Basal sliding under grounded ice, v_b, is described by a Weertman-Budd-type sliding law accounting for sub-melt sliding (Hindmarsh and Le Meur 2001) and the subglacial water-layer thickness (Kleiner and Humbert 2014, Calov et al. 2018):

$$v_\mathrm{b} = -C_\mathrm{b} \frac{\tau_\mathrm{b}^p}{N_\mathrm{b}^q} \,, \tag{7}$$

with

$$C_\mathrm{b} = C_\mathrm{b}^0 \exp\left(\frac{T_\mathrm{b}'}{\gamma}\right) \left[1 + c\left(1 - \exp\left(-\frac{H_\mathrm{w}}{H_\mathrm{w}^0}\right)\right)\right] . \tag{8}$$

In Eq. (7), C_b is the sliding function, τ_b the basal drag (shear stress), N_b the basal normal stress (ice stress minus water pressure, counted positive for compression), and p and q are the sliding exponents. In Eq. (8), C_b^0 is the sliding coefficient, T_b' the basal temperature relative to pressure melting (in °C, always ≤ 0°C), γ the sub-melt-sliding parameter, c the coefficient for water-layer-enhanced basal sliding, H_w the subglacial water-layer thickness and H_w^0 the threshold water-layer thickness. Optionally, the simulated ice sheet can be divided into $n = 1 \ldots N$ regions, for which individual basal sliding coefficients $(C_\mathrm{b}^0)_n$ are set. We do this for the $N = 18$ IMBIE-2016 basins (Rignot and Mouginot 2016, The IMBIE Team 2018) (see below, Sect. 3.2.3). The water-layer thickness H_w is computed by a steady-state routing scheme for subglacial water that receives its input from the basal melting rate under grounded ice (Le Brocq et al. 2006, 2009).

The sliding law (7) features a singularity for $N_\mathrm{b} \to 0$ (when grounded ice becomes nearly floating close to the grounding line). To avoid this, we impose a limiter such that $N_\mathrm{b} \geq 0.35 P_\mathrm{b}$, where $P_\mathrm{b} = \rho g H$ is the hydrostatic pressure of the ice column (ice thickness H). However, the limiter is only applied for the SIA. For the SStA, the sliding law appears in its inverse form (solved for τ_b), so that the singularity does not appear, and the limiter is thus not required (SICOPOLIS parameter SLIDE_LAW = 3).

Quantity	Value
Density of ice, ρ	$910\,\mathrm{kg\,m^{-3}}$
Density of sea water, ρ_sw	$1028\,\mathrm{kg\,m^{-3}}$
Gravitational acceleration, g	$9.81\,\mathrm{m\,s^{-2}}$
Length of year, 1 a	31 556 926 s
Power-law exponent, n	3
Residual stress, σ_0	10 kPa
Flow enhancement factor, E	grounded ice: 5, floating ice: 1
Melting temperature at low pressure, T_0	273.16 K
Clausius-Clapeyron gradient, β	$8.7 \times 10^{-4}\,\mathrm{K\,m^{-1}}$
Universal gas constant, R	$8.314\,\mathrm{J\,mol^{-1}K^{-1}}$
Heat conductivity of ice, κ	$9.828\,\mathrm{e}^{-0.0057\,T[\mathrm{K}]}\,\mathrm{W\,m^{-1}K^{-1}}$
Specific heat of ice, c	$(146.3 + 7.253\,T[\mathrm{K}])\,\mathrm{J\,kg^{-1}K^{-1}}$
Latent heat of ice, L	$3.35 \times 10^5\,\mathrm{J\,kg^{-1}}$
Sliding exponents, (p, q)	$(3, 2)$
Sub-melt-sliding parameter, γ	1°C
Coefficient for water-layer-enhanced basal sliding, c	9
Threshold water-layer thickness, H_w^0	5 mm
Density × specific heat of the lithosphere, $\rho_\mathrm{l} c_\mathrm{l}$	$2000\,\mathrm{kJ\,m^{-3}K^{-1}}$
Heat conductivity of the lithosphere, κ_l	$3\,\mathrm{W\,m^{-1}K^{-1}}$
Thickness of the thermal upper boundary layer of the lithosphere, H_lt	2 km
Flexural stiffness of the lithosphere, K_l	$10^{25}\,\mathrm{N\,m}$
Asthenosphere density, ρ_a	$3300\,\mathrm{kg\,m^{-3}}$
Time lag for the relaxing asthenosphere, τ_a	3000 a

Table 1: Physical parameters used for the simulations of this study.

The bed topography is Bedmap2 (Fretwell et al. 2013). Glacial isostatic adjustment (GIA) is included using an elastic-lithosphere–relaxing-asthenosphere (ELRA) model (parameters by Sato and Greve 2012). The geothermal heat flux is by Martos et al. (2017), applied at the base of the thermal lithosphere layer (rather than directly at the ice base) to account for the thermal inertia of the lithosphere (Ritz 1987). The physical parameters are listed in Table 1.

3 Initialization via paleoclimatic spin-up

A crucial prerequisite for future projections is a reasonable initial state of the ice sheet regarding ice geometry, surface velocities and englacial temperature (Goelzer et al. 2018, Seroussi et al. 2019). Here, we produce this initial state by carrying out a paleoclimatic spin-up over a full glacial cycle (140 ka) until the year 1990 CE (which corresponds to the time $t = 0$).

3.1 Climate forcing

The climatic forcing for the spin-up consists of time-dependent distributions of the surface temperature and precipitation. Like in the study by Sato and Greve (2012), the mean annual and mean summer surface temperatures (T_{ma} and T_{ms}, respectively) are decomposed into present-day spatial distributions plus a purely time-dependent anomaly $\Delta T(t)$,

$$\begin{aligned} T_{\mathrm{ma}}(h,\phi,t) &= T_{\mathrm{ma}}^{\mathrm{present}}(h,\phi) + \Delta T(t)\,, \\ T_{\mathrm{ms}}(h,\phi,t) &= T_{\mathrm{ms}}^{\mathrm{present}}(h,\phi) + \Delta T(t)\,, \end{aligned} \tag{9}$$

where t is time and ϕ geographical latitude. The present-day parameterizations are by Fortuin and Oerlemans (1990),

$$T_{\mathrm{ma}}^{\mathrm{present}} = \begin{cases} 7.405 - 0.014285\,h - 0.180\,\phi\,, & \text{for } h > 1500\,\mathrm{m}\,, \\ 36.689 - 0.005102\,h - 0.725\,\phi\,, & \text{for } 200\,\mathrm{m} < h \le 1500\,\mathrm{m}\,, \\ 49.642 - 0.943\,\phi\,, & \text{for } h \le 200\,\mathrm{m}\,, \end{cases} \tag{10}$$

$$T_{\mathrm{ms}}^{\mathrm{present}} = 16.81 - 0.00692\,h - 0.27937\,\phi\,, \tag{11}$$

where temperatures are in °C, surface elevations in m AMSL (above mean sea level) and latitudes in °S (counted positive). The time-dependent anomaly $\Delta T(t)$ results from the Vostok δD record converted to temperature with the relation by Petit et al. (1999).

We equate the present-day precipitation distribution $P^{\mathrm{present}}(\lambda,\phi)$ (where λ is geographical longitude) to the surface accumulation data by Arthern et al. (2006), Le Brocq et al. (2010). For any other time t, the precipitation $P(\lambda,\phi,t)$ is computed by P^{present} and a temperature-dependent factor via the parameterization by Huybrechts et al. (2007). Conversion from precipitation to snowfall rate (solid precipitation) is done on a monthly-mean basis using the linear function by Marsiat (1994).

Surface melting is parameterized by Reeh's (1991) positive degree day (PDD) method, supplemented by the semi-analytical solution for the PDD integral by Calov and Greve (2005). The PDD factors are $\beta_{\mathrm{ice}} = 8\,\mathrm{mm\,WE\,d^{-1}\,°C^{-1}}$ and $\beta_{\mathrm{snow}} = 3\,\mathrm{mm\,WE\,d^{-1}\,°C^{-1}}$ for ice and snow melt, respectively (where WE means water equivalent). Furthermore, the standard deviation of short-term, statistical air temperature fluctuations is $\sigma = 5°\mathrm{C}$, the saturation factor for the formation of superimposed ice is $P_{\max} = 0.6$, and we apply an empirical firn-warming correction due to refreezing melt water with a coefficient $\mu = 9.7155\,\mathrm{d\,°C\,(mm\,WE)^{-1}}$ (Reeh 1991).

For the part of the spin-up sequence prior to 2 ka ago with 32 and 16 km resolution (see Sect. 3.2 below), we use the parameterization for ice-shelf basal melting by Greve and Galton-Fenzi (2017) (SICOPOLIS parameter FLOATING_ICE_BASAL_MELTING = 5).

It takes the melt rate as a function of both the depth of ice below mean sea level and ocean temperatures outside the ice-shelf fronts at 500 m depth, tuned differently for eight Antarctic sectors. However, for the most recent 2 ka (8 km resolution), we switch to the "ISMIP6 standard approach" (SICOPOLIS parameter FLOATING_ICE_BASAL_MELTING = 6). This is a non-local quadratic melt-rate parameterization for the 18 IMBIE-2016 sectors (Rignot and Mouginot 2016, The IMBIE Team 2018), where the two sectors feeding the Ross ice shelf and the two sectors feeding the Filchner–Ronne ice shelf are combined, leaving 16 distinct sectors. The thermal forcing at the ice–ocean interface is derived by extrapolating the oceanic fields into the ice-shelf cavities. This melt-rate parameterization and its calibration by observations is described in detail by Jourdain et al. (2020). In both cases, no time dependence is considered; the parameterizations are kept fixed at their forms valid for present-day conditions during the entire model time of the spin-up. Over the abyssal ocean, defined by a threshold sea-bed elevation of −2500 m AMSL, we prescribe a large melt rate of 10 m WE a^{-1} to avoid that ice shelves spread out over these areas.

We describe ice-shelf calving by a 50-m thickness threshold. Any floating ice at the calving front that is thinner than this threshold is assumed to calve off instantaneously (Sato and Greve 2012).

3.2 Spin-up sequence

3.2.1 32 km resolution, $t = -140 \ldots -9$ ka

(1) Simulation ant32_b2_spinup22_init001a

Short simulation over 0.01 a, starting from the observed present-day topography, no basal sliding, glacial temperature anomaly $\Delta T = -6.864$°C (Vostok value for $t = -135$ ka). The initial temperature field is computed by the Robin (1955) solution for grounded ice columns with positive SMB and a linear profile otherwise (SICOPOLIS parameter TEMP_INIT = 4). Time steps: $\Delta t = 0.01$ a (for dynamics and topography), $\Delta t_{\text{temp}} = 0.01$ a (for thermodynamics), $\Delta t_{\text{wss}} = 0.01$ a (for steady-state displacement of the elastic lithosphere). The purpose of this run is to produce a slightly smoothed present-day topography (surface $h_{\text{target}}(x, y)$, bed $b_{\text{target}}(x, y)$) of the Antarctic ice sheet that serves as a target for the nudging technique of run (2).

(2) Simulation ant32_b2_spinup22_fixtopo

Time $t = -140 \ldots -9$ ka, starting from the output of run (1). Time steps: $\Delta t = 1$ a, $\Delta t_{\text{temp}} = 2$ a, $\Delta t_{\text{wss}} = 100$ a. Basal sliding with a constant sliding parameter $C_{\text{b}}^0 = 2.5\,\text{m}\,\text{a}^{-1}\,\text{Pa}^{-1}$ after −135 ka. During the first 5 ka (prior to −135 ka), basal sliding is ramped up as follows (Rückamp et al. 2019):

Introducing a non-dimensionalized time valid for the first 5 ka:

$$\tilde{t} = \frac{t - (-140\,\text{ka})}{5\,\text{ka}} \quad (\,\text{thus}\ \tilde{t} \in [0, 1]\,)\,, \tag{12}$$

gradual increase of the sliding coefficient by the quintic function (4):

$$C_{\text{b}}^0 \to f_5(\tilde{t})\, C_{\text{b}}^0\,. \tag{13}$$

The computed topography (surface $h(x, y)$, bed $b(x, y)$) is continuously nudged towards the output of run (1) by first solving the normal evolution equations for the bed and the ice thickness (e.g., Greve and Blatter 2009, Eqs. (5.55) and (8.5)) and then applying the relaxation equations

$$\frac{\partial h}{\partial t} = -\frac{h - h_{\text{target}}}{\tau_{\text{relax}}}\,, \tag{14}$$

$$\frac{\partial b}{\partial t} = -\frac{b - b_{\text{target}}}{\tau_{\text{relax}}}\,, \tag{15}$$

with a relaxation time of $\tau_{\text{relax}} = 100\,\text{a}$ (Rezvanbehbahani et al. 2019, Rückamp et al. 2019). This nudging is equivalent to applying an SMB correction (Aschwanden et al. 2013, 2016, Calov et al. 2018), which is diagnosed by the model.

3.2.2 16 km resolution, $t = -9 \ldots -2$ ka

(3) Simulation ant16_b2_spinup22_init001a

Similar to run (1): short simulation over 0.01 a, starting from the observed present-day topography, no basal sliding, temperature anomaly $\Delta T = -6.864°\text{C}$. Time steps: $\Delta t = 0.01\,\text{a}$, $\Delta t_{\text{temp}} = 0.01\,\text{a}$, $\Delta t_{\text{wss}} = 0.01\,\text{a}$. Purpose: to produce a slightly smoothed present-day topography that serves as a target for the nudging technique of run (4).

(4) Simulation ant16_b2_spinup22_fixtopo

Time $t = -9 \ldots -2\,\text{ka}$, starting from the resolution-doubled output of run (2) at $t = -9\,\text{ka}$. Time steps: $\Delta t = 0.1\,\text{a}$, $\Delta t_{\text{temp}} = 1\,\text{a}$, $\Delta t_{\text{wss}} = 10\,\text{a}$. Basal sliding with a constant sliding parameter $C_{\text{b}}^0 = 2.5\,\text{m}\,\text{a}^{-1}\,\text{Pa}^{-1}$. The computed topography is continuously nudged towards the output of run (3) as described above for run (2) [Eqs. (14), (15) and accompanying text].

3.2.3 8 km resolution, $t = -2 \ldots 0$ ka

(5) Simulation ant08_b2_spinup25_init10a

Similar to runs (1) and (3): short simulation over 10 a, starting from the observed present-day topography, no basal sliding, temperature anomaly $\Delta T = -6.864°\text{C}$. Time steps: $\Delta t = 0.02\,\text{a}$, $\Delta t_{\text{temp}} = 0.02\,\text{a}$, $\Delta t_{\text{wss}} = 1\,\text{a}$. Purpose: to produce a slightly smoothed present-day topography that serves as a target for the nudging technique of runs (6) and (7).

(6) Simulation ant08_b2_spinup25_fixtopo

Time $t = -2 \ldots -0\,\text{ka}$, starting from the resolution-doubled output of run (4) at $t = -2\,\text{ka}$. Time steps: $\Delta t = 0.05\,\text{a}$, $\Delta t_{\text{temp}} = 0.5\,\text{a}$, $\Delta t_{\text{wss}} = 10\,\text{a}$. Basal sliding with a constant sliding parameter $C_{\text{b}}^0 = 2.5\,\text{m}\,\text{a}^{-1}\,\text{Pa}^{-1}$. The computed topography is continuously nudged towards the output of run (5) as described above for run (2) [Eqs. (14), (15) and accompanying text].

(7) Simulations ant08_b2_spinup25_fixtopo-{01,02,03,04,05,06}

Each of these six runs reads the output of run (6) at $t = -100\,\mathrm{a}$ and runs until $t = 0$. Time steps: $\Delta t = 0.05\,\mathrm{a}$, $\Delta t_{\mathrm{temp}} = 0.5\,\mathrm{a}$, $\Delta t_{\mathrm{wss}} = 10\,\mathrm{a}$. The basal sliding coefficients $(C_{\mathrm{b}}^0)_n^k$ ($n = 1 \ldots 18$) are iteratively adjusted for the 18 IMBIE-2016 basins (Rignot and Mouginot 2016, The IMBIE Team 2018), to achieve optimum agreement between simulated and observed surface velocities in the basins. The index k counts the iterations. The starting value (iteration no. $k = 0$) is the value from run (6), $(C_{\mathrm{b}}^0)_n^0 = 2.5\,\mathrm{m\,a^{-1}\,Pa^{-1}}$. Except for the basal sliding, the set-up is the same as that of run (6).

The k-th iteration of the run is called ant08_b2_spinup25_fixtopo-k. For each basin n, a regression line through the origin with the slope a_n^k is computed:

$$(v_{\mathrm{sim}})_n^k = a_n^k\,(v_{\mathrm{obs}})_n^k\,, \tag{16}$$

where $v_{\{\mathrm{sim,obs}\}}$ are the simulated and observed surface velocities, respectively. Only velocities within $[10\,\mathrm{m\,a^{-1}}, 3000\,\mathrm{m\,a^{-1}}]$ for which the simulation predicts grounded ice with a temperate base are considered. Taking the decimal logarithm yields

$$y = x + b\,, \tag{17}$$

with $y = \lg\,(v_{\mathrm{sim}})_n^k$, $x = \lg\,(v_{\mathrm{obs}})_n$ and $b = \lg\,a_n^k$ (indices k and n dropped for brevity). This describes a line with a slope of unity and an intercept of b. The latter is computed by the least-squares method:

$$\sum_{i=1}^{I}(y_i - (x_i + b))^2 \to \min\,, \tag{18}$$

where the index $i = 1 \ldots I$ counts the grid points in the respective basin. This yields [via $(\partial/\partial b)\,(\sum \ldots) \stackrel{!}{=} 0$]

$$b = \frac{1}{I}\sum_{i=1}^{I}(y_i - x_i)\,, \tag{19}$$

which is the arithmetic mean of the misfit between simulated and observed logarithmic velocities. The slope a_n^k is then

$$a_n^k = 10^b\,. \tag{20}$$

It is used to update the basal sliding coefficients for the next iteration according to

$$(C_{\mathrm{b}}^0)_n^{k+1} = \frac{(C_{\mathrm{b}}^0)_n^k}{a_n^k}\,, \tag{21}$$

with a lower bound of $(C_{\mathrm{b}}^0)_{\mathrm{min}} = 0.1\,\mathrm{m\,a^{-1}\,Pa^{-1}}$. The target of the iterations is to get the slopes a_n^k as close to unity as possible.

The procedure is stopped after $k = 6$ iterations (ant08_b2_spinup25_fixtopo-06), when the overall slope (for the entire ice sheet) has reached the interval $[0.95, 1.05]$: $a_{\mathrm{all}}^6 = 1.0473$. Figure 4a demonstrates that the scheme has converged well; further iterations

would not lead to a significant improvement of the fit. The regional basal siding coefficients (Fig. 4b) show a great variability. The largest values occur in basins No. 9, 8 (draining from West and East Antarctica, respectively, into the Ross ice shelf), 11 (containing the Pine Island and Thwaites glaciers) and 17 (draining from East Antarctica into the Filchner ice shelf). By contrast, six basins (Nos. 1, 4, 6, 10, 12, 14) reach or come close to the lower bound of $0.1\,\mathrm{m\,a^{-1}\,Pa^{-1}}$, thus showing very little basal sliding.

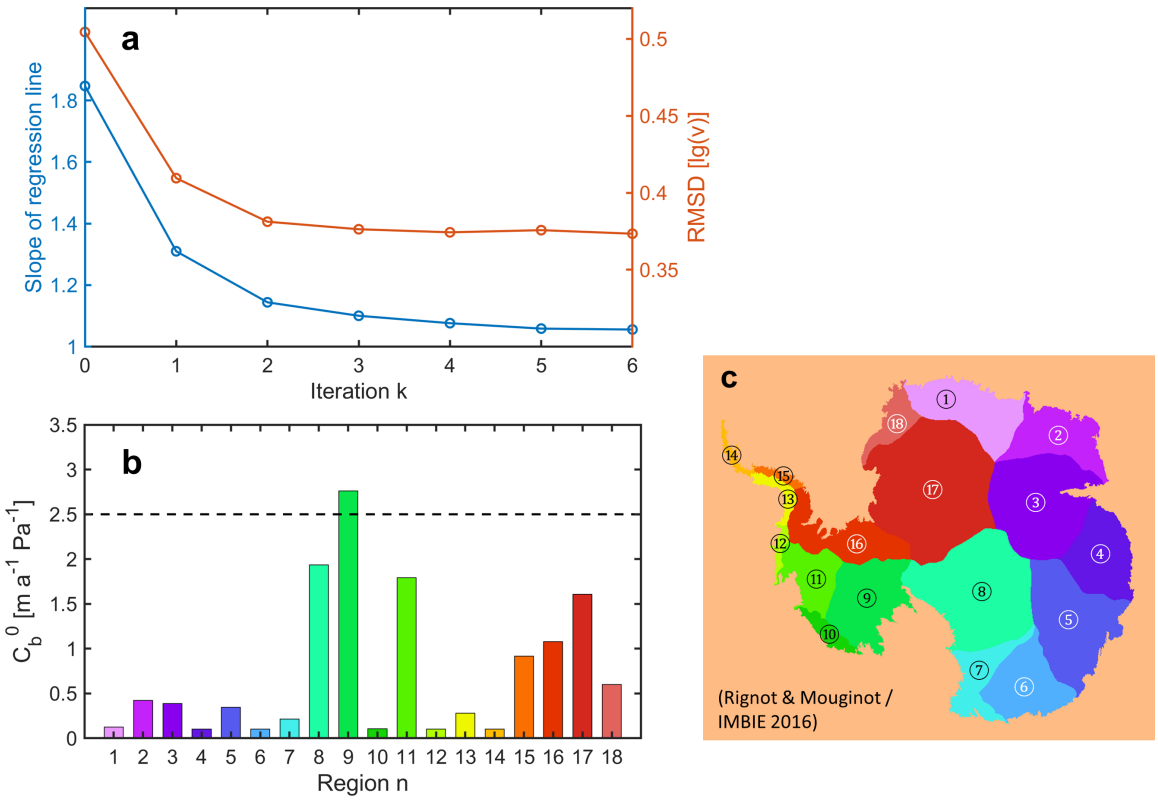

Figure 4: (a) Slope a^k_{all} of the regression line for the entire ice sheet and RMSD (root mean square deviation) of the logarithmic surface velocity $\lg(v)$ (in $\mathrm{m\,a^{-1}}$) for the entire ice sheet after k iterations. (b) Resulting basal sliding coefficients $(C_{\mathrm{b}}^0)_n$ for the 18 IMBIE-2016 basins (Rignot and Mouginot 2016, The IMBIE Team 2018). (c) Location of the basins, marked by circled numbers that correspond to the region number n in panel (b).

(8) Simulation ant08_b2_spinup25-06

Time $t = -500 \ldots 0\,\mathrm{a}$, starting from the output of run (6) at $t = -500\,\mathrm{a}$. Time steps: $\Delta t = 0.02\,\mathrm{a}$, $\Delta t_{\mathrm{temp}} = 0.5\,\mathrm{a}$, $\Delta t_{\mathrm{wss}} = 10\,\mathrm{a}$. Basal sliding coefficients as determined from the final run (7). Free evolution of the ice topography. Temporally constant SMB correction applied, which is the 1960–1989 average SMB correction diagnosed by the nudging technique of the final run (7).

(9) Simulation ant08_b2_spinup25-06_120a

Time $t = -120 \ldots 0\,\mathrm{a}$, re-run of the last 120 a of run (8) with annual output of scalar and 2D fields as requested by the ISMIP6 protocol. The final state of this run is our initial ice sheet for the year 1990 CE.

3.3 Simulated initial (1990 CE) ice sheet

The spin-up sequence produces an initial ice sheet with a total volume of $26.264 \times 10^6\,\mathrm{km}^3$, a volume above flotation of 57.149 m SLE (sea-level equivalent), a grounded ice area of $12.098 \times 10^6\,\mathrm{km}^2$ and a floating ice area of $1.593 \times 10^6\,\mathrm{km}^2$. Due to the nudging technique applied during the entire period of the spin-up except for the last 500 years, the simulated ice thickness agrees well with its observed counterpart (Fig. 5). In the interior ice sheet, the misfit is typically of the order of 10 m only. Closer to the coast, larger misfits occur, typically in areas of fast-flowing ice streams like the Pine Island and Thwaites glaciers (too thin) or the Lambert glacier (too thick). The RMSD (root mean square deviation) for the whole ice sheet, including the ice shelves, is 69.3 m.

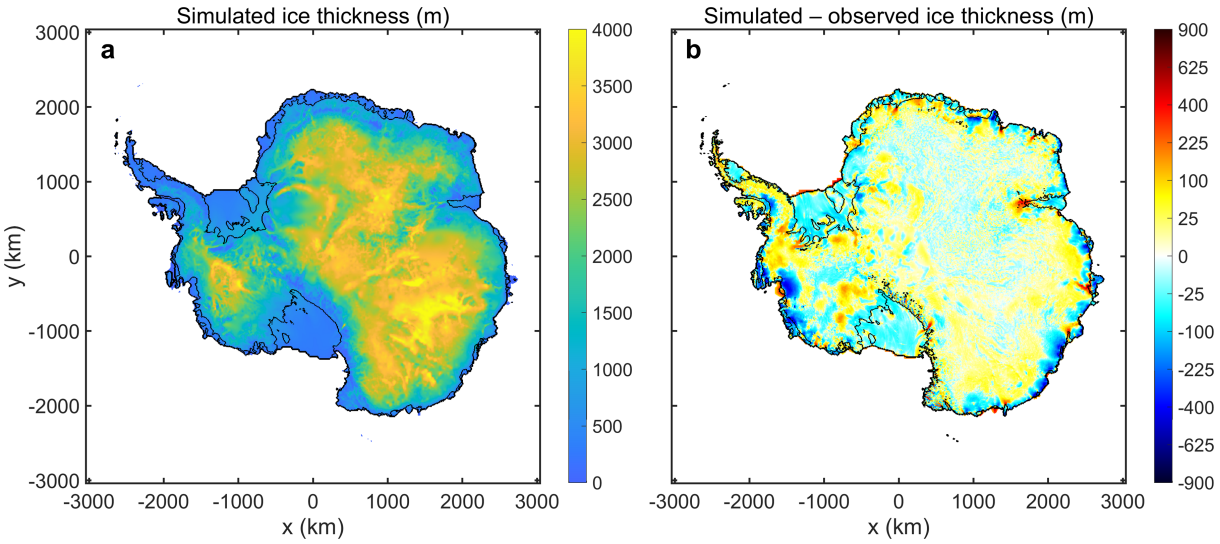

Figure 5: Spin-up simulation: (a) Simulated initial (1990 CE) ice thickness. (b) Simulated minus observed (Fretwell et al. 2013) ice thickness on a square-root scale.

The simulated surface-velocity field for the initial state of the Antarctic ice sheet is shown in Fig. 6. Overall, it agrees well with the observations. The large-scale structure, as well as most of the smaller-scale features, in particular the major ice streams and outlet glaciers, are well reproduced. The RMSD for the whole ice sheet, including the ice shelves, is $101.3\,\mathrm{m\,a}^{-1}$.

From the last 30 years of the spin-up, we extract a 1960–1989 reference climatology, which is shown in Fig. 7. The SMB is the sum of the prescribed snowfall minus melting rate (Sect. 3.1) and the 1960–1989 mean SMB correction that results from the nudging technique (Sect. 3.2). This yields desert-like conditions in central East Antarctica, more Greenland-like conditions in central West Antarctica and generally larger positive SMB values near the coast. However, patches of negative SMB also occur, for instance, inland of Siple Coast or in the area of Lambert glacier. A conspicuous positive anomaly is present in the Pine-Island/Thwaites area, where the topography nudging method adds several metres per year of ice to prevent the area from destabilizing. The ST distribution results from the parameterization described in Sect. 3.1 and shows the expected pattern with very low temperatures in central East Antarctica, moderately low temperatures in central West Antarctica and milder conditions near the coast.

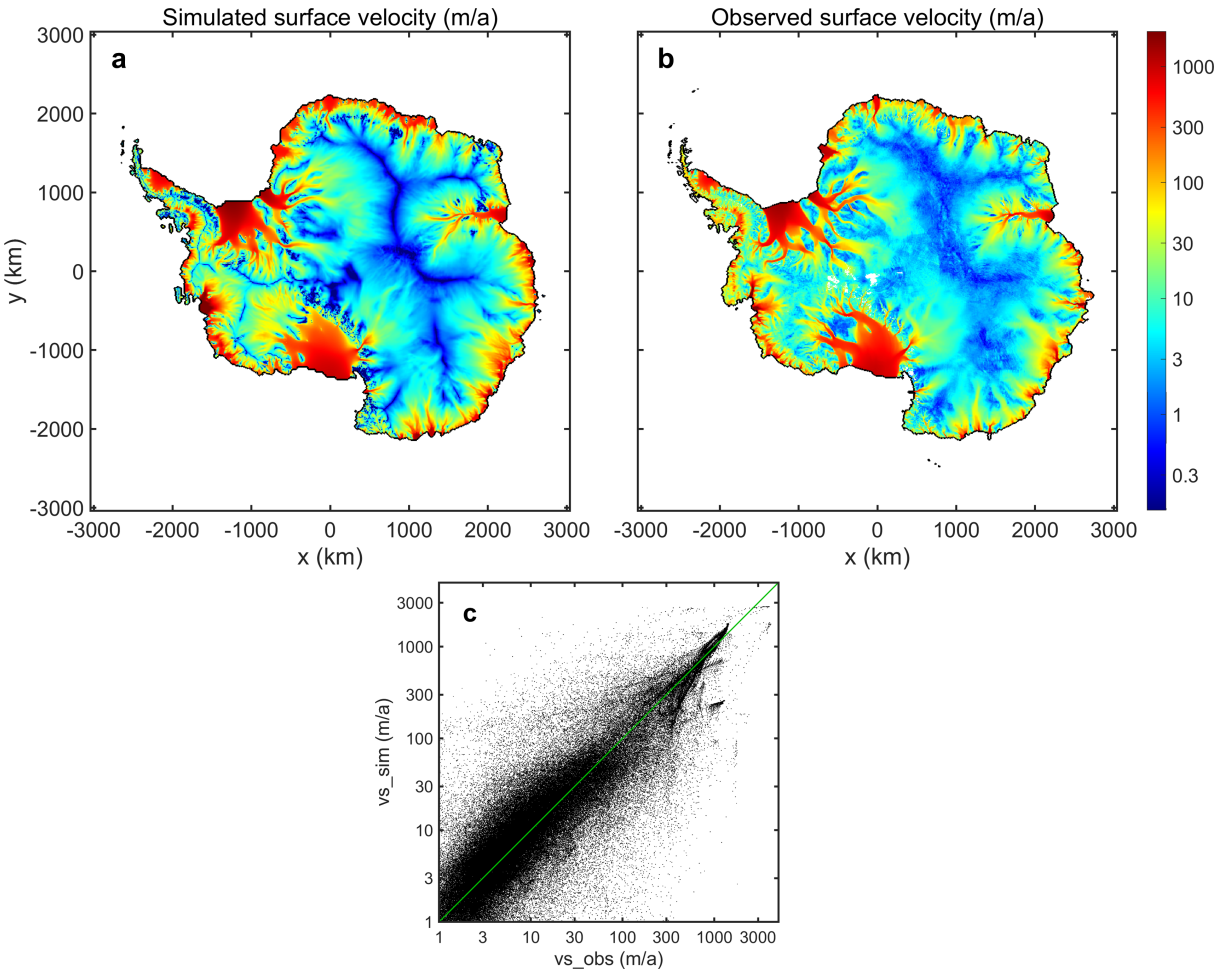

Figure 6: Spin-up simulation: (a) Simulated initial (1990 CE) vs. (b) observed (Rignot et al. 2011, 2017, Mouginot et al. 2012) surface-velocity fields. (c) Scatter plot of simulated vs. observed surface velocities. All velocities are shown on a logarithmic scale.

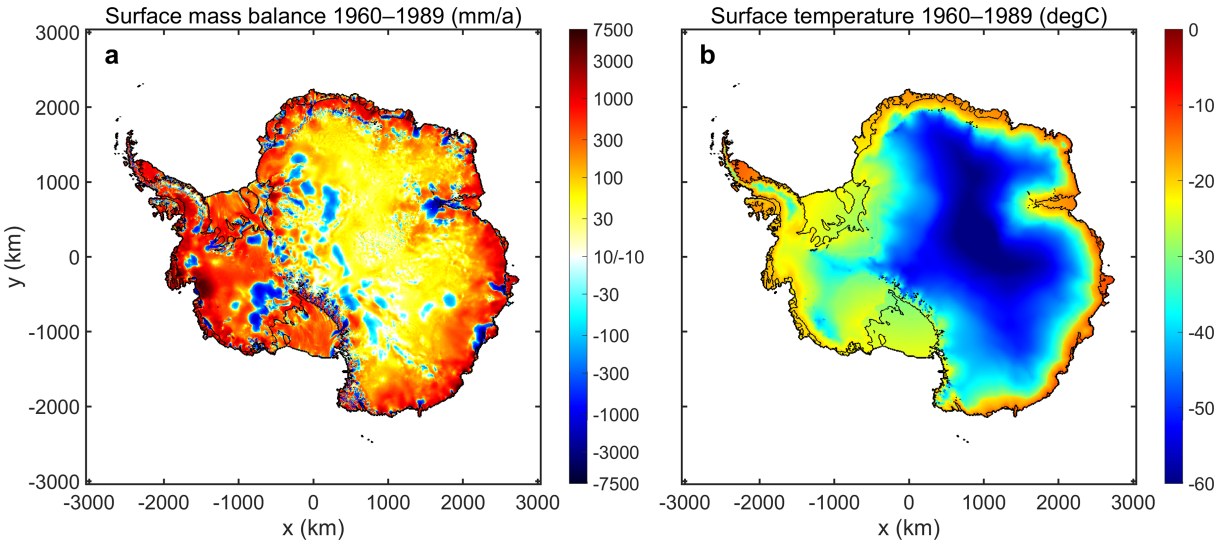

Figure 7: 1960–1989 reference climatology. (a) Surface mass balance (on a combined positive/negative logarithmic scale, in ice equivalents). (b) Surface temperature.

4 ISMIP6 future projections for Antarctica

We now describe the experiments that run from the initialization date 1990 CE into the future. For all experiments, we use the regional basal sliding coefficients determined by the spin-up runs (7) (Fig. 4b), and the time steps are the same as those of the spin-up runs (8) and (9): $\Delta t = 0.02\,\mathrm{a}$, $\Delta t_{\mathrm{temp}} = 0.5\,\mathrm{a}$, $\Delta t_{\mathrm{wss}} = 10\,\mathrm{a}$.

4.1 Control runs, schematic experiments, historical run

We carry out a constant-climate control run ('ctrl') from 1990 until the end of 2100. It uses the ice sheet for 1990 that results from the spin-up as initial conditions. The time-independent forcing consists of our 1960–1989 reference climatology and the oceanic forcing from the ISMIP6 standard approach (see Sect. 3.1) for the present day. Under these conditions, the ice sheet remains nearly stable, featuring only a small mass loss of 13.1 mm SLE during the 111 years model time (not shown).

We repeat the initMIP-Antarctica experiments 'asmb' and 'abmb' (Seroussi et al. 2019) with the settings of this study. The set-up is that of ctrl, plus a time-dependent, schematic anomaly for the SMB (asmb) and the ice-shelf basal melt (abmb), respectively. This produces a notable response of the ice sheet (Fig. 8, black dashed and dotted lines): The increased precipitation of asmb leads to a mass gain of 146.8 mm SLE, while the increased ice-shelf basal melt of abmb leads to a mass loss of 94.2 mm SLE. While the quantitative interpretability of these numbers is limited due to the schematic nature of the experiments, they illustrate well two major, counteracting effects that can cause changes of the Antarctic ice sheet in the near future.

The historical run ('hist') bridges the gap between our initialization time 1990 and the start date of the projections in January 2015. Like ctrl, asmb and abmb, it starts from the 1990 ice sheet that results from the spin-up. Following the ISMIP6 recommendation (tinyurl.com/ismip6-wiki-ais, last accessed 2020-08-12), the climate forcing consists of the 1960–1989 reference climatology, NorESM1-M RCP8.5 SMB and ST anomalies as well as NorESM1-M RCP8.5 oceanic thermal forcing. The ice sheet reacts only slightly, losing 1.2 mm SLE mass during the 25 years model time (Fig. 8, thick black solid line).

From the last 20 years of the historical run, we extract a 1995–2014 reference climatology (SMB, ST). It is very similar to the 1960–1989 one (Fig. 7) and thus not shown separately.

Following the ISMIP6 protocol, we conduct a second control run for January 2015 – December 2100, the same period that is used for the actual future climate experiments (see Sect. 4.2 below). This projection control run ('ctrl_proj') starts from the final state of the historical run. It uses the 1995–2014 reference climatology and the oceanic forcing resulting from the ISMIP6 standard approach (see Sect. 3.1) for the present day. Similar to ctrl, the ice sheet remains nearly stable, showing only a slight mass loss of 1.0 mm SLE during the 86 years model time (Fig. 8, thin black solid line).

The SICOPOLIS names of the simulations described above are ant08_b2_future25-06_{ctrl,asmb,abmb,hist,ctrl_proj}.

4.2 Future climate experiments

The future climate experiments start from the final state of the historical run, and the model time is from January 2015 until December 2100. Their atmospheric forcing consists of the 1995–2014 reference climatology (see above), plus space-time-dependent anomalies for the SMB and the ST. For the core (Tier 1) experiments, these anomalies were derived from three selected CMIP5 global climate models (GCMs) (Barthel et al. 2020). For the extended ensemble (Tier 2), three additional CMIP5 GCMs were added, and a further extension (also Tier 2) includes four CMIP6 GCMs, the latter mainly chosen on the basis of early availability. The ISMIP6 projections focus on the pessimistic "business as usual" scenarios RCP8.5 (CMIP5) or SSP5-8.5 (CMIP6). However, some experiments are also devised for the optimistic RCP2.6 (CMIP5) or SSP1-2.6 (CMIP6) scenarios that represent substantial emissions reductions. [RCP: Representative Concentration Pathway, SSP: Shared Socioeconomic Pathway.]

#	exp_id	Scenario	GCM	Ocean forcing	Ice-shelf fracture	
5	exp05	RCP8.5	NorESM1-M	Medium	No	Core experiments (Tier 1)
6	exp06	RCP8.5	MIROC-ESM-CHEM	Medium	No	
7	exp07	RCP2.6	NorESM1-M	Medium	No	
8	exp08	RCP8.5	CCSM4	Medium	No	
9	exp09	RCP8.5	NorESM1-M	High	No	
10	exp10	RCP8.5	NorESM1-M	Low	No	
12	exp12	RCP8.5	CCSM4	Medium	Yes	
13	exp13	RCP8.5	NorESM1-M	PIGL-Medium	No	
A5	expA5	RCP8.5	HadGEM2-ES	Medium	No	Extended ensemble (Tier 2)
A6	expA6	RCP8.5	CSIRO-Mk3.6.0	Medium	No	
A7	expA7	RCP8.5	IPSL-CM5A-MR	Medium	No	
A8	expA8	RCP2.6	IPSL-CM5A-MR	Medium	No	
B6	expB6	SSP5-8.5	CNRM-CM6-1	Medium	No	CMIP6 extension (Tier 2)
B7	expB7	SSP1-2.6	CNRM-CM6-1	Medium	No	
B8	expB8	SSP5-8.5	UKESM1-0-LL	Medium	No	
B9	expB9	SSP5-8.5	CESM2	Medium	No	
B10	expB10	SSP5-8.5	CNRM-ESM2-1	Medium	No	

Table 2: ISMIP6-Antarctica Tier-1 and 2 future climate experiments discussed in this study. See Nowicki et al. (2020) for references for the GCMs. The SICOPOLIS names of these simulations are ant08_b2_future25-06_<exp_id>.

The oceanic forcing is not based on anomalies, but on absolute values of the oceanic fields produced by the climate models. They are interpolated into the ice-shelf cavities, which yields the space-time-dependent thermal forcing at the ice–ocean interface. It is converted to ice-shelf basal melt rates by the same non-local quadratic melt-rate parameterization that we used for the last 2 ka of the spin-up ("ISMIP6 standard approach", Sect. 3.1). In addition to the normal, "medium" calibration, "high" and "low" calibra-

tions are tested, as well as a calibration in which only observed basal-melt values near the grounding line of the Pine Island ice shelf are used ("PIGL-medium") (Jourdain et al. 2020).

In one experiment, ice-shelf fracture triggered by surface melting is accounted for. This is implemented by a time-dependent ice-shelf-collapse mask, computed on the assumption that collapse occurs following a 10-year period with annual surface melt above 725 mm (Trusel et al. 2015).

An overview of the ISMIP6 Tier-1 and Tier-2 experiments is given in Table 2. There are 17 experiments, 14 of which are for RCP8.5/SSP5-8.5 and three for RCP2.6/SSP1-2.6. In three experiments, the impact of different calibrations of the parameterization for ice-shelf basal melting is tested, and one experiment includes ice-shelf hydrofracture. [Further 14 experiments employ an "open forcing", in which the choice of the parameterization for ice-shelf basal melting is left to the discretion of the individual modellers. We have not conducted them with SICOPOLIS, so that they are not considered here.] For more details on the forcing, we refer to Nowicki et al. (2020) and Seroussi et al. (2020).

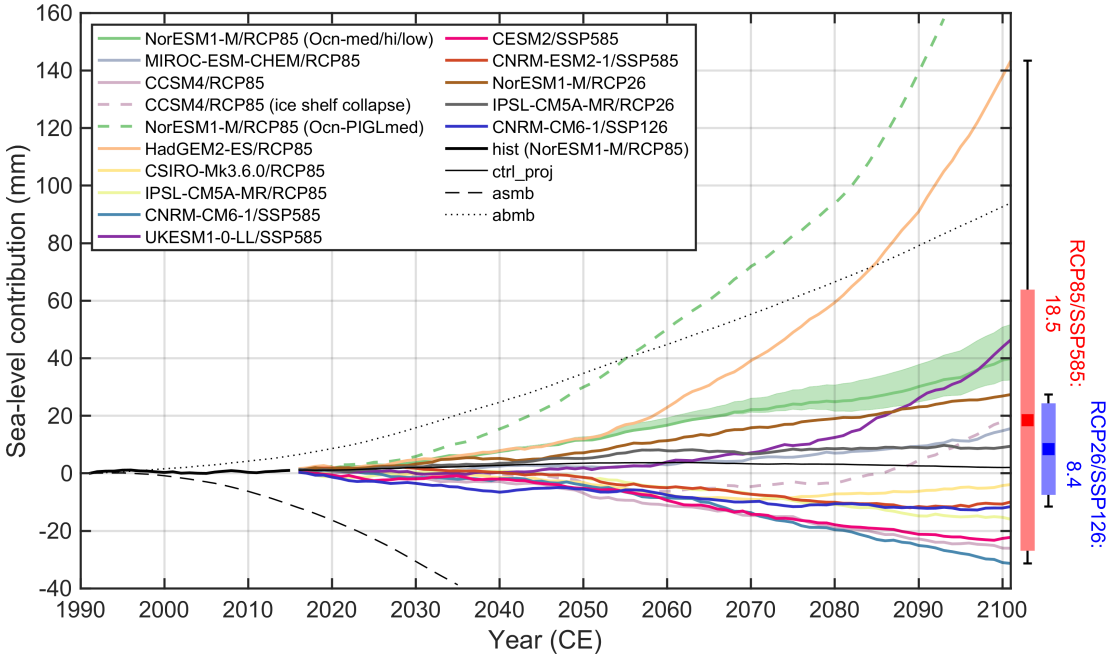

Figure 8: ISMIP6-Antarctica historical run (hist), projection control run (ctrl_proj), schematic initMIP experiments (asmb, abmb) and Tier-1 and 2 future climate experiments: Simulated ice mass change, counted positively for loss and expressed as sea-level contribution. The red and blue boxes to the right show the mean ± 1-sigma ranges for RCP8.5/SSP5-8.5 and RCP2.6/SSP1-2.6, respectively; the whiskers show the corresponding full ranges.

The contribution to sea-level change produced by these experiments is shown in Fig. 8 (coloured lines). Over the entire period from 1990 until 2100, it is 18.5 ± 45.4 mm (mean ± 1-sigma uncertainty) for the RCP8.5/SSP5-8.5 experiments (excluding Exp. #13, see below) and 8.4 ± 15.9 mm for the RCP2.6/SSP1-2.6 experiments. Thus, for both pathways, mass losses and gains occur, depending on the GCM forcing. For RCP8.5/SSP5-8.5, 6 out of 14 experiments, and for RCP2.6/SSP1-2.6, 1 out of 3 experiments produce

slight mass gains (negative contributions to sea-level change), the most extreme case being Exp. #B6 (CNRM-CM6-1/SSP5-8.5) with a value of −31.1 mm SLE. On the other end of the range, the largest mass loss is produced by Exp. #A5 (HadGEM2-ES/RCP8.5), 143.6 mm SLE. As already discussed in Sect. 4.1, this is due to the interplay between increasing precipitation, leading to a mass gain, and increasing ice-shelf basal melt, leading to a mass loss. These counteracting drivers have different relative strengths in the different GCM results, which leads to the inconsistent response of the ice sheet.

The influence of the calibration of the parameterization for ice-shelf basal melt is explored by Exps. #5, 9, 10 (NorESM1-M/RCP8.5 with "medium", "high" and "low" calibrations, respectively). The results are shown by the green line and green-shaded region in Fig. 8. By 2100, the simulated mass loss is $40.0\,^{+11.9}_{-7.4}$ mm SLE. Thus, the uncertainty due to these three calibrations is notable, but smaller than the uncertainty due to the GCM forcings. A more extreme test is Exp. #13, which is NorESM1-M/RCP8.5 with the "PIGL-medium" calibration described above. During the 86 years model time, this leads to an, on average, ~ 2 times larger total ice-shelf basal melting than for Exp. #5. It has a pronounced effect on the mass loss of the ice sheet: By 2100, it is 216.7 mm SLE compared to the initial 1990 state, and 176.6 mm SLE larger than that of Exp.#5. This is the largest mass loss of the ensemble of simulations, thus highlighting the great sensitivity of the Antarctic ice sheet to oceanic forcing.

Exps. #8 and 12 (CCSM4/RCP8.5) investigate the influence of ice-shelf hydrofracture as described above (included in Exp. #12). Exp. #8 is actually one of the cases that produce a mass gain of the ice sheet. Adding ice-shelf hydrofracture via the time-dependent collapse mask in Exp. #12 reverts this behaviour to a mass loss, the difference between the two experiments amounting to 46.1 mm SLE. Thus, the process can act as a significant amplifier of the mass loss of the Antarctic ice sheet.

For a more detailed analysis of the future climate experiments, including results from other ice-sheet models, regional patterns etc., we refer to the ISMIP6 community papers by Seroussi et al. (2020) and Payne et al. (2020).

5 Summary

We described the ISMIP6 future projections for the Antarctic ice sheet with the model SICOPOLIS, with a focus on the model-specific methods and set-up. Our paleoclimatic spin-up over 140 ka with successively refining resolution employed a topography nudging technique and an optimization of the basal sliding coefficients for 18 different basins to ensure a good match between the observed and the simulated initial (1990 CE) ice sheet. A historical run, forced by NorESM1-M/RCP8.5, brought the modelled ice sheet from this initial state to the projection start date January 2015. Our ensemble of 17 ISMIP6 Tier-1 and Tier-2 future climate experiments, forced by ten different CMIP5 and CMIP6 GCMs for two different pathways (RCP8.5/SSP5-8.5, RCP2.6/SSP1-2.6), forked off from there and was run until the end of the 21st century (December 2100).

The response of the Antarctic ice sheet is mainly determined by two counteracting processes. Increasing ocean temperatures entail increasing ice-shelf basal melting, leading to a mass loss (positive contribution to sea-level rise). By contrast, increasing precipitation over the ice sheet leads to a mass gain (negative contribution to sea-level rise). The

ensemble means for both pathways are small, positive sea-level contributions. However, uncertainties in the calibration of the parameterization for ice-shelf basal melting and hydrofracturing of ice shelves can potentially lead to a significantly larger mass loss of the ice sheet.

Additional ISMIP6 Tier-3 experiments have already been defined (ISMIP6 Steering Committee, personal communication 2019). They include experiments with atmosphere-only and ocean-only forcing, more sensitivity tests for the oceanic forcing and further experiments including ice-shelf hydrofracture. Further, we are planning to carry out simulations extending beyond 2100 to assess the longer-term response of the Antarctic ice sheet to climate-change conditions.

Acknowledgements

We thank the Climate and Cryosphere (CliC) effort, which provided support for ISMIP6 through sponsoring of workshops, hosting the ISMIP6 website and wiki, and promoting ISMIP6. We acknowledge the World Climate Research Programme, which, through its Working Group on Coupled Modelling, coordinated and promoted CMIP5 and CMIP6. We thank the climate modelling groups for producing their model output and making it available; the Earth System Grid Federation (ESGF) for archiving the CMIP data and providing access to it; the University at Buffalo for ISMIP6 data distribution and upload; and the multiple funding agencies who support CMIP5, CMIP6, and ESGF. We thank the ISMIP6 steering committee, the ISMIP6 model selection group and ISMIP6 dataset preparation group for their continuous engagement in defining ISMIP6. This is ISMIP6 contribution No. 21.

Ralf Greve and Ayako Abe-Ouchi were supported by Japan Society for the Promotion of Science (JSPS) KAKENHI grant Nos. JP16H02224, JP17H06104 and JP17H06323. Reinhard Calov was funded by the PalMod project (PalMod 1.1 and 1.3 with grants 01LP1502C and 01LP1504D) of the German Federal Ministry of Education and Research (BMBF).

References

Arakawa, A. and Lamb, V. R.: Computational design of the basic dynamical processes of the UCLA general circulation model, in: Methods in Computational Physics Vol. 17, edited by Chang, J., pp. 173–265, Academic Press, New York, NY, USA, 1977.

Arthern, R. J., Winebrenner, D. P., and Vaughan, D. G.: Antarctic snow accumulation mapped using polarization of 4.3-cm wavelength microwave emission, Journal of Geophysical Research: Atmospheres, 111, D06 107, https://doi.org/10.1029/2004JD005667, 2006.

Aschwanden, A., Aðalgeirsdóttir, G., and Khroulev, C.: Hindcasting to measure ice sheet model sensitivity to initial states, The Cryosphere, 7, 1083–1093, https://doi.org/10.5194/tc-7-1083-2013, 2013.

Aschwanden, A., Fahnestock, M. A., and Truffer, M.: Complex Greenland outlet glacier flow captured, Nature Communications, 7, 10 524, https://doi.org/10.1038/ncomms10524, 2016.

Barthel, A., Agosta, C., Little, C. M., Hattermann, T., Jourdain, N. C., Goelzer, H., Nowicki, S., Seroussi, H., Straneo, F., and Bracegirdle, T. J.: CMIP5 model selection for ISMIP6 ice sheet model forcing: Greenland and Antarctica, The Cryosphere, 14, 855–879, https://doi.org/10.5194/tc-14-855-2020, 2020.

Bernales, J., Rogozhina, I., Greve, R., and Thomas, M.: Comparison of hybrid schemes for the combination of shallow approximations in numerical simulations of the Antarctic Ice Sheet, The Cryosphere, 11, 247–265, https://doi.org/10.5194/tc-11-247-2017, 2017.

Blatter, H. and Greve, R.: Comparison and verification of enthalpy schemes for polythermal glaciers and ice sheets with a one-dimensional model, Polar Science, 9, 196–207, https://doi.org/10.1016/j.polar.2015.04.001, 2015.

Calov, R. and Greve, R.: A semi-analytical solution for the positive degree-day model with stochastic temperature variations, Journal of Glaciology, 51, 173–175, https://doi.org/10.3189/172756505781829601, 2005.

Calov, R., Beyer, S., Greve, R., Beckmann, J., Willeit, M., Kleiner, T., Rückamp, M., Humbert, A., and Ganopolski, A.: Simulation of the future sea level contribution of Greenland with a new glacial system model, The Cryosphere, 12, 3097–3121, https://doi.org/10.5194/tc-12-3097-2018, 2018.

Cuffey, K. M. and Paterson, W. S. B.: The Physics of Glaciers, Elsevier, Amsterdam, The Netherlands etc., 4th edn., 2010.

Eyring, V., Bony, S., Meehl, G. A., Senior, C. A., Stevens, B., Stouffer, R. J., and Taylor, K. E.: Overview of the Coupled Model Intercomparison Project Phase 6 (CMIP6) experimental design and organization, Geoscientific Model Development, 9, 1937–1958, https://doi.org/10.5194/gmd-9-1937-2016, 2016.

Fortuin, J. P. F. and Oerlemans, J.: Parameterization of the annual surface temperature and mass balance of Antarctica, Annals of Glaciology, 14, 78–84, https://doi.org/10.3189/S0260305500008302, 1990.

Fretwell, P., Pritchard, H. D., Vaughan, D. G., Bamber, J. L., Barrand, N. E., Bell, R., Bianchi, C., Bingham, R. G., Blankenship, D. D., Casassa, G., Catania, G., Callens, D., Conway, H., Cook, A. J., Corr, H. F. J., Damaske, D., Damm, V., Ferraccioli, F., Forsberg, R., Fujita, S., Gim, Y., Gogineni, P., Griggs, J. A., Hindmarsh, R. C. A., Holmlund, P., Holt, J. W., Jacobel, R. W., Jenkins, A., Jokat, W., Jordan, T., King, E. C., Kohler, J., Krabill, W., Riger-Kusk, M., Langley, K. A., Leitchenkov, G., Leuschen, C., Luyendyk, B. P., Matsuoka, K., Mouginot, J., Nitsche, F. O., Nogi, Y., Nost, O. A., Popov, S. V., Rignot, E., Rippin, D. M., Rivera, A., Roberts, J., Ross, N., Siegert, M. J., Smith, A. M., Steinhage, D., Studinger, M., Sun, B., Tinto, B. K., Welch, B. C., Wilson, D., Young, D. A., Xiangbin, C., and Zirizzotti, A.: Bedmap2: improved ice bed, surface and thickness datasets for Antarctica, The Cryosphere, 7, 375–393, https://doi.org/10.5194/tc-7-375-2013, 2013.

Goelzer, H., Nowicki, S., Edwards, T., Beckley, M., Abe-Ouchi, A., Aschwanden, A., Calov, R., Gagliardini, O., Gillet-Chaulet, F., Golledge, N. R., Gregory, J., Greve, R., Humbert, A., Huybrechts, P., Kennedy, J. H., Larour, E., Lipscomb, W. H., Le clec'h, S., Lee, V., Morlighem, M., Pattyn, F., Payne, A. J., Rodehacke, C., Rückamp, M., Saito, F., Schlegel, N., Seroussi, H., Shepherd, A., Sun, S., van de Wal, R., and Ziemen, F. A.: Design and results of the ice sheet model initialisation experiments initMIP-Greenland: an ISMIP6 intercomparison, The Cryosphere, 12, 1433–1460, https://doi.org/10.5194/tc-12-1433-2018, 2018.

Greve, R.: Thermomechanisches Verhalten polythermer Eisschilde – Theorie, Analytik, Numerik, Doctoral thesis, Department of Mechanics, Darmstadt University of Technology, Germany, https://doi.org/10.5281/zenodo.3815324, 1995.

Greve, R.: A continuum-mechanical formulation for shallow polythermal ice sheets, Philosophical Transactions of the Royal Society A, 355, 921–974, https://doi.org/10.1098/rsta.1997.0050, 1997a.

Greve, R.: Application of a polythermal three-dimensional ice sheet model to the Greenland ice sheet: Response to steady-state and transient climate scenarios, Journal of Climate, 10, 901–918, https://doi.org/10.1175/1520-0442(1997)010⟨0901:AOAPTD⟩2.0.CO;2, 1997b.

Greve, R. and Blatter, H.: Dynamics of Ice Sheets and Glaciers, Springer, Berlin, Germany etc., https://doi.org/10.1007/978-3-642-03415-2, 2009.

Greve, R. and Blatter, H.: Comparison of thermodynamics solvers in the polythermal ice sheet model SICOPOLIS, Polar Science, 10, 11–23, https://doi.org/10.1016/j.polar.2015.12.004, 2016.

Greve, R. and Galton-Fenzi, B.: InitMIP-Antarctica experiments with the ice sheet model SICOPOLIS, Presentation No. MIS10-01, JpGU-AGU Joint Meeting, Makuhari Messe, Chiba, Japan, 24 May 2017, 2017.

Greve, R. and SICOPOLIS Developer Team: SICOPOLIS v5.1, Zenodo, https://doi.org/10.5281/zenodo.3727511, 2019.

Greve, R., Chambers, C., and Calov, R.: ISMIP6 future projections for the Greenland ice sheet with the model SICOPOLIS, Technical report, Zenodo, https://doi.org/10.5281/zenodo.3971251, 2020.

Hindmarsh, R. C. A. and Le Meur, E.: Dynamical processes involved in the retreat of marine ice sheets, Journal of Glaciology, 47, 271–282, https://doi.org/10.3189/172756501781832269, 2001.

Huybrechts, P., Rybak, O., Pattyn, F., Ruth, U., and Steinhage, D.: Ice thinning, upstream advection, and non-climatic biases for the upper 89% of the EDML ice core from a nested model of the Antarctic ice sheet, Climate of the Past, 3, 577–589, https://doi.org/10.5194/cp-3-577-2007, 2007.

Jourdain, N. C., Asay-Davis, X., Hattermann, T., Straneo, F., Seroussi, H., Little, C. M., and Nowicki, S.: A protocol for calculating basal melt rates in the ISMIP6 Antarctic ice sheet projections, The Cryosphere, 14, https://doi.org/10.5194/tc-14-xxxx-2020, in press, 2020.

Kleiner, T. and Humbert, A.: Numerical simulations of major ice streams in western Dronning Maud Land, Antarctica, under wet and dry basal conditions, Journal of Glaciology, 60, 215–232, https://doi.org/10.3189/2014JoG13J006, 2014.

Le Brocq, A. M., Payne, A. J., and Siegert, M. J.: West Antarctic balance calculations: impact of flux-routing algorithm, smoothing algorithm and topography, Computers & Geosciences, 32, 1780–1795, https://doi.org/10.1016/j.cageo.2006.05.003, 2006.

Le Brocq, A. M., Payne, A. J., Siegert, M. J., and Alley, R. B.: A subglacial water-flow model for West Antarctica, Journal of Glaciology, 55, 879–888, https://doi.org/10.3189/002214309790152564, 2009.

Le Brocq, A. M., Payne, A. J., and Vieli, A.: An improved Antarctic dataset for high resolution numerical ice sheet models (ALBMAP v1), Earth System Science Data, 2, 247–260, https://doi.org/10.5194/essd-2-247-2010, 2010.

Lliboutry, L. and Duval, P.: Various isotropic and anisotropic ices found in glaciers and polar ice caps and their corresponding rheologies, Annales Geophysicae, 3, 207–224, 1985.

Marsiat, I.: Simulation of the northern hemisphere continental ice sheets over the last glacial-interglacial cycle: Experiments with a latitude-longitude vertically integrated ice sheet model coupled to zonally averaged climate model, Paleoclimates: Data and Modelling, 1, 59–98, 1994.

Martos, Y. M., Catalán, M., Jordan, T. A., Golynsky, A., Golynsky, D., Eagles, G., and Vaughan, D. G.: Heat flux distribution of Antarctica unveiled, Geophysical Research Letters, 44, 11 417–11 426, https://doi.org/10.1002/2017GL075609, 2017.

Mouginot, J., Scheuchl, B., and Rignot, E.: Mapping of ice motion in Antarctica using synthetic-aperture radar data, Remote Sensing, 4, 2753–2767, https://doi.org/10.3390/rs4092753, 2012.

Nowicki, S., Goelzer, H., Seroussi, H., Payne, A. J., Lipscomb, W. H., Abe-Ouchi, A., Agosta, C., Alexander, P., Asay-Davis, X. S., Barthel, A., Bracegirdle, T. J., Cullather, R., Felikson, D., Fettweis, X., Gregory, J. M., Hattermann, T., Jourdain, N. C., Kuipers Munneke, P., Larour, E., Little, C. M., Morlighem, M., Nias, I., Shepherd, A., Simon, E., Slater, D., Smith, R. S., Straneo, F., Trusel, L. D., van den Broeke, M. R., and van de Wal, R.: Experimental protocol for sea level projections from ISMIP6 stand-alone ice sheet models, The Cryosphere, 14, 2331–2368, https://doi.org/10.5194/tc-14-2331-2020, 2020.

Nowicki, S. M. J., Payne, A., Larour, E., Seroussi, H., Goelzer, H., Lipscomb, W., Gregory, J., Abe-Ouchi, A., and Shepherd, A.: Ice Sheet Model Intercomparison Project (ISMIP6) contribution to CMIP6, Geoscientific Model Development, 9, 4521–4545, https://doi.org/10.5194/gmd-9-4521-2016, 2016.

Payne, A. J., Nowicki, S., Abe-Ouchi, A., Agosta, C., Alexander, P., Albrecht, T., Asay-Davis, X., Barthel, A., Calov, R., Chambers, C., Choi, Y., Cullather, R., Cuzzone, J., Dumas, C., Edwards, T., Felikson, D., Fettweis, X., Goelzer, H., Gladstone, R., Golledge, N. R., Gregory, J. M., Greve, R., Hatterman, T., Hoffman, M. J., Humbert, A., Huybrechts, P., Jourdain, N. C., Kleiner, T., Larour, E., Le clec'h, S., Lee, V., Leguy, G., Lipscomb, W. H., Little, C. M., Lowry, D. P., Morlighem, M., Nias, I., Pattyn, F., Pelle, T., Price, S., Quiquet, A., Reese, R., Rückamp, M., Schlegel, N.-J., Seroussi, H., Shepherd, A., Simon, E., Slater, D., Smith, R., Straneo, F., Sun, S., Tarasov, L., Trusel, L. D., Van Breedam, J., van de Wal, R., van den Broeke, M., Winkelmann, R., Zhao, C., Zhang, T., and Zwinger, T.: Contrasting contributions to future sea level under CMIP5 and CMIP6 scenarios from the Greenland and Antarctic ice sheets, Geophysical Research Letters, submitted, 2020.

Petit, J. R., Jouzel, J., Raynaud, D., Barkov, N. I., Barnola, J. M., Basile, I., Bender, M., Chappellaz, J., Davis, M., Delaygue, G., Delmotte, M., Kotlyakov, V. M., Legrand, M., Lipenkov, V. Y., Lorius, C., Pepin, L., Ritz, C., Saltzman, E., and Stievenard, M.: Climate and atmospheric history of the past 420,000 years from the Vostok ice core, Antarctica, Nature, 399, 429–436, https://doi.org/10.1038/20859, 1999.

Reeh, N.: Parameterization of melt rate and surface temperature on the Greenland ice sheet, Polarforschung, 59, 113–128, 1991.

Rezvanbehbahani, S., Stearns, L. A., van der Veen, C. J., Oswald, G. K. A., and Greve, R.: Constraining the geothermal heat flux in Greenland at regions of radar-detected basal water, Journal of Glaciology, 65, 1023–1034, https://doi.org/10.1017/jog.2019.79, 2019.

Rignot, E. and Mouginot, J.: Antarctica and Greenland drainage basin and ice sheet definitions, IMBIE 2016, URL `http://imbie.org/imbie-2016/drainage-basins/`, 2016.

Rignot, E., Mouginot, J., and Scheuchl, B.: Ice flow of the Antarctic ice sheet, Science, 333, 1427–1430, https://doi.org/10.1126/science.1208336, 2011.

Rignot, E., Mouginot, J., and Scheuchl, B.: MEaSUREs InSAR-based Antarctica ice velocity map, version 2, NASA NSIDC Distributed Active Archive Center, Boulder, Colorado, USA, https://doi.org/10.5067/D7GK8F5J8M8R, 2017.

Ritz, C.: Time dependent boundary conditions for calculation of temperature fields in ice sheets, in: The Physical Basis of Ice Sheet Modelling, edited by Waddington, E. D. and Walder, J. S., IAHS Publication No. 170, pp. 207–216, IAHS Press, Wallingford, UK, 1987.

Robin, G. de Q.: Ice movement and temperature distribution in glaciers and ice sheets, Journal of Glaciology, 2, 523–532, https://doi.org/10.3198/1955JoG2-18-523-532, 1955.

Rückamp, M., Greve, R., and Humbert, A.: Comparative simulations of the evolution of the Greenland ice sheet under simplified Paris Agreement scenarios with the models SICOPOLIS and ISSM, Polar Science, 21, 14–25, https://doi.org/10.1016/j.polar.2018.12.003, 2019.

Sato, T. and Greve, R.: Sensitivity experiments for the Antarctic ice sheet with varied sub-ice-shelf melting rates, Annals of Glaciology, 53, 221–228, https://doi.org/10.3189/2012AoG60A042, 2012.

Seroussi, H., Nowicki, S., Simon, E., Abe-Ouchi, A., Albrecht, T., Brondex, J., Cornford, S., Dumas, C., Gillet-Chaulet, F., Goelzer, H., Golledge, N. R., Gregory, J. M., Greve, R., Hoffman, M. J., Humbert, A., Huybrechts, P., Kleiner, T., Larour, E., Leguy, G., Lipscomb, W. H., Lowry, D., Mengel, M., Morlighem, M., Pattyn, F., Payne, A. J., Pollard, D., Price, S. F., Quiquet, A., Reerink, T. J., Reese, R., Rodehacke, C. B., Schlegel, N.-J., Shepherd, A., Sun, S., Sutter, J., Van Breedam, J., van de Wal, R. S. W., Winkelmann, R., and Zhang, T.: InitMIP-Antarctica: an ice sheet model initialization experiment of ISMIP6, The Cryosphere, 13, 1441–1471, https://doi.org/10.5194/tc-13-1441-2019, 2019.

Seroussi, H., Nowicki, S., Payne, A. J., Goelzer, H., Lipscomb, W. H., Abe-Ouchi, A., Agosta, C., Albrecht, T., Asay-Davis, X., Barthel, A., Calov, R., Cullather, R., Dumas, C., Galton-Fenzi, B. K., Gladstone, R., Golledge, N., Gregory, J. M., Greve, R., Hatterman, T., Hoffman, M. J., Humbert, A., Huybrechts, P., Jourdain, N. C., Kleiner, T., Larour, E., Leguy, G. R., Lowry, D. P., Little, C. M., Morlighem, M., Pattyn, F., Pelle, T., Price, S. F., Quiquet, A., Reese, R., Schlegel, N.-J., Shepherd, A., Simon, E., Smith, R. S., Straneo, F., Sun, S., Trusel, L. D., Van Breedam, J., van de Wal, R. S. W., Winkelmann, R., Zhao, C., Zhang, T., and Zwinger, T.: ISMIP6 Antarctica: a multi-model ensemble of the Antarctic ice sheet evolution over the 21st century, The Cryosphere, 14, https://doi.org/10.5194/tc-14-xxxx-2020, in press, 2020.

The IMBIE Team: Mass balance of the Antarctic Ice Sheet from 1992 to 2017, Nature, 558, 219–222, https://doi.org/10.1038/s41586-018-0179-y, 2018.

Trusel, L. D., Frey, K. E., Das, S. B., Karnauskas, K. B., Kuipers Munneke, P., van Meijgaard, E., and van den Broeke, M. R.: Divergent trajectories of Antarctic surface melt under two twenty-first-century climate scenarios, Nature Geoscience, 8, 927–932, https://doi.org/10.1038/ngeo2563, 2015.